Magnetic resonance imaging of water ascent in embolized xylem vessels of grapevine stem segments

Mingtao Wang[1], Melvin T. Tyree[2,3], and Roderick E. Wasylishen[1,4]

[1]*Department of Chemistry, University of Alberta, Edmonton, Alberta, Canada T6G 2G2;* [2]*Department of Renewable Resources, University of Alberta, Edmonton, Alberta, Canada T6G 2H1; and* [3]*College of Forestry, Northwest A&F University, Yangling, Shaanxi, China.* *Received 25 January 2013, accepted 3 May 2013.*

Wang, M., Tyree, M. T. and Wasylishen, R. E. 2013. **Magnetic resonance imaging of water ascent in embolized xylem vessels of grapevine stem segments**. Can. J. Plant Sci. **93**: 879–893. Temporal and spatial information about water refilling of embolized xylem vessels and the rate of water ascent in these vessels is critical for understanding embolism repair in intact living vascular plants. High-resolution ^{1}H magnetic resonance imaging (MRI) experiments have been performed on embolized grapevine stem segments while they were subjected to refilling at two different applied water pressures in order to investigate these important aspects of embolism repair. Magnetic resonance imaging difference images show that vessels located near the bark tend to refill faster than do inner ones, suggesting that vessel position within the cross section of the stem may affect the refilling process within the vessel. An MRI method for determining the water ascent velocity in each individual embolized xylem vessel is presented. At ambient pressure, the water ascent velocity ranges from 0.0090 to 0.60 mm min^{-1}, but increases to a range of 0.016 to 0.70 mm min^{-1} at 9.8 kPa above ambient pressure. A steady-state bubble model that offers analytical solutions of the water ascent velocity in embolized xylem vessels is presented; model calculations show that if other parameters are held constant, water ascent velocity is influenced by vessel diameter and position.

Key words: Magnetic resonance imaging, water ascent velocity in grapevine stems, steady-state bubble model, embolized xylem vessels, *Vitis labrusca* L.

Wang, M., Tyree, M. T. et Wasylishen, R. E. 2013. **Imagerie par résonance magnétique de l'ascension de l'eau dans les vaisseaux obstrués du xylème des segments de vigne**. Can. J. Plant Sci. **93**: 879–893. On a absolument besoin de données temporelles et spatiales sur l'ascension de l'eau dans les vaisseaux obstrués du xylème ainsi que sur la vitesse à laquelle l'eau monte dans ces vaisseaux pour comprendre comment les plantes vasculaires vivantes se remettent d'une embolie. Les auteurs ont examiné des segments de vigne obstrués par IRM ^{1}H à haute résolution durant leur remplissage à deux pressions différentes, cela afin d'étudier ces aspects importants de la réparation des embolies. Les images IRM différentielles révèlent que les vaisseaux situés près de l'écorce ont tendance à se remplir plus vite que ceux situés plus à l'intérieur, ce qui laisse croire que l'emplacement du vaisseau dans la coupe transversale de la tige est susceptible d'affecter son remplissage. Les auteurs proposent une méthode IRM permettant d'établir la vitesse à laquelle l'eau grimpe dans chaque vaisseau du xylème obstrué. À pression ambiante, cette vitesse varie de 0,0090 à 0,60 mm par minute, mais elle augmente à 0,016 à 0,70 mm par minute à 9,8 kPa au-dessus de la pression ambiante. Suit la présentation d'un modèle à bulle de l'état stable permettant de résoudre les problèmes associés à l'analyse de la vitesse d'ascension de l'eau dans les vaisseaux du xylème obstrués; les calculs réalisés avec ce modèle indiquent que, lorsque les autres paramètres sont constants, la vitesse d'ascension de l'eau subit l'influence du diamètre et de l'emplacement des vaisseaux.

Mots clés: Imagerie par résonance magnétique, vitesse d'ascension de l'eau dans les vignes, modèle à bulle de l'état stable, vaisseaux du xylème obstrués, *Vitis labrusca* L.

Water transport in xylem vessels is vital to vascular plants (Raven 1977; Tyree and Sperry 1989; Tyree and Zimmermann 2002; Brodbribb 2009); however, this process can be disrupted if water cavitates in individual vessels (Tyree and Sperry 1989; Tyree and Zimmermann 2002). When a xylem vessel becomes embolized (i.e., air-filled) after a cavitation event, it can no longer transport water until it is repaired (Holbrook and Zwieniecki 1999; Tyree et al. 1999). The mechanism by which plants repair their embolized xylem vessels is only partly resolved (Yang and Tyree 1992; Salleo et al. 1996; Canny 1998; McCully et al. 1998; Zwieniecki and Holbrook 1998; Pate and Canny 1999; Zwieniecki and Holbrook 2000; Melcher et al. 2001; Clearwater and Goldstein 2005; Salleo et al. 2009).

Experimental methods, such as hydraulic conductivity measurements (Tyree and Yang 1992; Hacke and Sperry 2003), cryo-scanning electron microscopy (Facette et al. 2001), acoustic emission testing (Borghetti et al. 1991;

[4]*Corresponding author (e-mail: Roderick.wasylishen@ualberta.ca).*

Abbreviations: **i.d.**, inner diameter; **MRI**, magnetic resonance imaging; **MSME**, multiple slice multiple spin echo; **NMR**, nuclear magnetic resonance; **ROI**, region of interest; T_1, spin-lattice relaxation time; T_2, spin-spin relaxation time; **TR**, repetition time

Laschimke et al. 2006), X-ray imaging (Lee and Kim 2008), high-resolution computed tomography (McElrone et al. 2012) and theoretical modeling (Yang and Tyree 1992) have been used to investigate embolism repair. Magnetic resonance imaging (MRI) is also well suited to investigate water in plants (Callaghan 1991, 2011; Kimmich 1997; Rokitta et al. 1999; Blümich 2000; Narasimhan and Jacobs 2005; Van As et al. 2009; Choat et al. 2010; Borisjuk et al. 2012; MacFall and Johnson 2012; Telkki 2012; Gruwel et al. 2013). For example, ^{1}H MRI experiments have been used to investigate the loss of xylem conductivity caused by *Xylella fastidiosa* infection and ethylene exposure (Pérez-Donoso et al. 2007), to image in vivo xylem vessel content in woody lianas (Clearwater and Clark 2003), and to study the dynamics of water transport in phloem and xylem tissues (Windt et al. 2006; Homan et al. 2007; Scheenen 2007) and in seedlings (Köckenberger et al. 1997) of plants. Previously, Holbrook et al. (2001) reported the successful use of ^{1}H MRI experiments to monitor the occurrence of cavitation and its repair in the stem of an intact, transpiring grape (*Vitis vinifera*).

Two types of embolism repair have been studied extensively in the past (Tyree and Zimmermann 2002): (1) refilling of vessels in early spring in dormant stems before leaf emergence and (2) repair in summer when leaves are present and water is flowing through some vessels to keep up with evaporation from the leaves, while others are refilling. In the former case the water in all vessels is under positive pressure (root pressure or stem pressure). In the latter case water in surrounding water-filled vessels is under negative pressure while embolized vessels are refilling by positive pressure. The most definitive study of the latter case used high resolution (1 μm) computer tomography of X-ray images to study the dynamics of refilling (Brodersen et al. 2010). In the present study we use lower-resolution MRI imaging (20 to 30 μm) to study refilling in simulated springtime conditions as explained below.

In 1992, the first models were tested to gain an understanding of how embolisms can collapse in excised dormant maple stems based on Fick's Law, Henry's Law and surface tension at air-water interfaces (Tyree and Yang 1992; Yang and Tyree 1992). These early studies documented embolism collapse indirectly through measured changes in hydraulic conductivity that results as embolisms disappear. The objective of this research is to revisit the old theories with the added power of MRI, which can image individual vessels, to see if the theory can explain the rate of bubble collapse in excised grape stem segments under well-controlled conditions.

In the work presented here, high-resolution ^{1}H MRI experiments were performed on grapevine stem segments to investigate the temporal and spatial patterns of water refilling of embolized xylem vessels. An MRI method was developed to determine the rate of collapse of air bubbles and movement of the meniscus, when the fluid pressure in the xylem is under experimental control and held to a value near to atmospheric pressure. Fluid pressure is easily controlled in excised stem segments, and we believe this is the first study to focus on velocity measurements of meniscus movement in biological systems, although such measurements have been undertaken for microchannels in silicon nitride chips (Yang et al. 2004). An enhanced understanding of events under controlled conditions (simulated springtime conditions) may allow us to better explain the quite different behavior of intact grapevines whereby vessels seem to refill when water is metastable (fluid pressure < -0.1 MPa) (Brodersen et al. 2010). Finally, we hope that the research described herein will increase the awareness of researchers in the plant science community of a powerful technique for studying water density in plants that is generally associated with medicine, MRI.

MATERIALS AND METHODS

Plant Materials

Stem segments 12–14 cm in length and 4–6 mm in diameter were collected from a Concord grapevine (*Vitis labrusca* L.) that had been allowed to grow for several years with no pruning. All stem segments were >1 yr old and had survived a full winter and had budded to form current year stems and leaves distal of the harvested segment. Embolism in the stems was induced by injecting air into one end of the stems for approximately 2 min with a pressure of >0.6 MPa, which embolized most of the vessels. After the embolization treatment, the stems were promptly subjected to water refilling and ^{1}H MRI measurements.

Magnetic Resonance Imaging RI Experiments

^{1}H MRI experiments were performed on the stems while they were refilling with water at two different xylem pressures, one at ambient pressure and the other at 9.8 kPa above ambient pressure, hereafter referred to as 9.8 kPa. The experimental setup is shown in Fig. 1a. The stem segment was positioned in the radio frequency birdcage coil with its basal end connected via water-filled tubing that ran through the MRI probe to a water-filled bottle whose height could be adjusted to achieve different water pressures. The top end of the stem segment was sealed by a water-filled compression fitting. Escape of air through open vessels was thereby prevented and gas trapped in vessels could only dissipate through dissolution, thus drawing in water from the base of the stem. In all experiments, the influx end of the stem segment was maintained approximately 40 mm below the center of the resonator (Fig. 1b).

A multiple-slice multiple spin-echo (MSME) MRI method (Graumann et al. 1986; De Deene and Baldock 2002) was used to acquire ^{1}H MRI images of the cross section of the stems and to determine the water ascent velocity in embolized xylem vessels. Using this technique, an axial slice package containing five 1.5-mm-thick slices with a 0.5-mm inter-slice gap was defined along

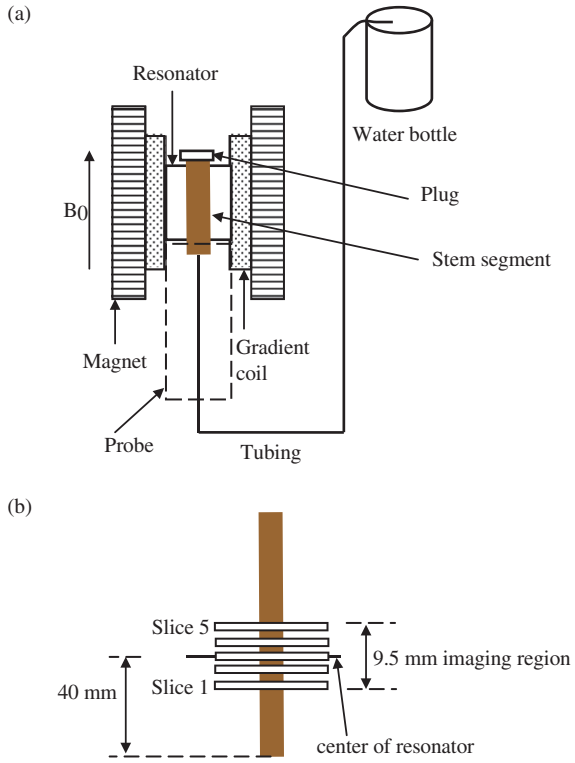

Fig. 1. Experimental setup for water refilling and ^{1}H MRI experiments (a). The plug on the distal end of the stem segment prevents bulk water movement through the segment so that water movement proceeds only as fast the embolisms dissolve. The geometric relationship between the water-stem surface and the center of the resonator, as well as the imaging region of the stems are shown in (b); note that portions of this figure are not drawn to scale. For ambient pressure measurement the water level in the water bottle was at the resonator level. For the 9.8 kPa experiments the water level was 1 m higher.

the stem such that slice number 1 was at the bottom and slice number 5 was at the top of the slice package (Fig. 1b). With this slice geometry and using an interleaved slice acquisition scheme, one expects to first observe the water meniscus in slice 1, and then up through slices 2, 3, 4 and 5, respectively. Since the motion of the meniscus was slow compared with the time required to acquire a given image, the use of interleaved data acquisition did not affect the conclusions about the motion of the meniscus. In principle, radial movement of air bubbles between vessels must pass through pit membrances, which requires a high pressure differential across the buuble meniscus $\geq 30\times$ the pressures applied in our experiments; hence, bubble movement between vessels was not considered in the analysis. Qualitatively, one can locate the water meniscus within each embolized xylem vessel by examining the five slice images acquired at any given refilling time. As the slice thickness and the interslice gap are known, the distance travelled by the meniscus between two different refilling times can be calculated. If a constant ascent velocity within the imaging region is assumed, its value can then be determined. Quantitatively, the signal intensity of the slices must be considered to determine the ascent velocity accurately.

The signal intensity for a ^{1}H MRI image acquired using a spin-echo pulse sequence is primarily weighted by ^{1}H relaxation times (e.g., T_1 and T_2) and its density (the amount of water in this case). For this particular problem, since the ^{1}H density in a refilling slice is changing as a function of time, the total acquisition time of an MRI image influences the signal intensity as each phase encoding step contributes differently to the total signal intensity of the final MRI image. As outlined below, each of these problems was considered.

^{1}H T_1 weighting of the signal intensity can largely be removed by using a repetition time (TR) of at least $3T_1$. In contrast, ^{1}H T_2 effects are more difficult to address. Factors affecting the latter for water in xylem vessels include the vessel diameter (Callaghan 1990; Araujo et al. 1993), the amount of water in the vessel, the presence of air bubbles, their geometry and influence on magnetic susceptibility, etc. (Callaghan 1990; Arbabi and Mastikhin 2012); consequently, a T_2 correction of the ^{1}H nuclear magnetic resonance (NMR) signal intensity is not feasible. However, for the slice geometry defined in Fig. 1b, the maximum difference in water content between two slices corresponds to 8 mm height of the water column within the same vessel. Considering that a typical xylem vessel in grapevine stems is much longer than 8 mm, that the bottom slice of the package is 35.25 mm from the bottom of the stem and that when the water meniscus is in slice number 1, a significant amount of water is already in the vessel, the difference in ^{1}H T_2 values for water in any two slices that are defined for a given xylem vessel is expected to be negligible.

Since many factors affect ^{1}H T_2 values, the echo time used in these experiments must be carefully optimized to minimize effects of varying T_2 times. In general, the longer the echo time, the larger the effect of susceptibility on relaxation times and thus on image amplitude. In principle, the effects of susceptibility could be minimized by using a single-point imaging spin echo (SE-SPI) scheme (Beyea et al. 2000) since this essentially removes the time evolution of the Hamiltonian. However, these SE-SPI experiments typically require long acquisition times that may result in loss of the temporal resolution of the ascent velocity and thus are not appropriate given the time resolution needed to observe bubble movement.

The effect of the acquisition time, i.e., the total experiment time to acquire an MRI image, on the signal intensity can be circumvented using a process that involves two different slices at two different refilling times. For a given vessel, let $S(t, n)$ represent the signal intensity of the ^{1}H MRI image of slice n at refilling time t. For a specific vessel, if the refilling is assumed to occur by the same process at two different observed slices, and if $S(t_1,n_1) = S(t_2,n_2)$ then the acquisition time imparts the

same effect on the signal intensity of the ^{1}H MRI images of these two different slices. Consequently, the ascent velocity, v, can be calculated as:

$$v = \frac{(n_2 - n_1)(l + \Delta l)}{t_2 - t_1} \quad (1)$$

where l and Δl denote the slice thickness and interslice gap, respectively.

For a given slice defined for a specific xylem vessel, $S(t,n)$ is a function of t with n fixed. Plotting $S(t,n)$ against t allows the construction of a curve that characterizes the relationship between the signal intensity and refilling time for this specific slice. Comparison of such curves for two different slices permits the determination of the time required for these two slices to acquire the same ^{1}H MRI signal intensity; this time can then be used to calculate the water ascent velocity in this specific embolized xylem vessel (vide infra).

High-resolution ^{1}H MRI experiments were performed with a 7.05 Tesla (300.17 MHz), vertical wide-bore (89 mm i.d.) superconducting magnet with a Bruker Avance 300 console, Micro-2.5 imaging accessory, and a 10 mm i.d. birdcage resonator. A micrograd ient set (40 mm i.d.) capable of 1.0 T m^{-1} was mounted in the magnet bore. The temperature of the gradient unit was maintained at 20°C using a water-cooling system provided by Bruker, and all MRI experiments were performed at room temperature (approximately 22°C). ^{1}H T_1 and T_2 values for water in individual xylem vessels at the normal water refilled state (i.e., before embolization treatment) were measured using saturation-recovery (Roscher et al. 1996; Markley et al. 1971) and spin-echo MRI experiments (Meiboom and Gill 1958), respectively. An MSME MRI pulse sequence was employed for all the MRI experiments with the following parameters: echo time = 10.6 ms, TR = 3000 ms, number of averages = 1, field of view = 6.0 mm × 6.0 mm, MTX = 256 × 256, slice thickness = 1.5 mm. ^{1}H MRI experiments were performed every 13 min once refilling of the embolized stems began (see below for details).

Steady-state Bubble Model

A steady-state bubble model assuming cylindrical symmetry and homogeneous vessel diameter is proposed. For simplicity, consider a vessel lumen somewhere inside a stem with no end walls, and an air bubble in the center of the stem/vessel with a distance L between the end of the bubble and the end of the stem (Fig. 2). The stem length and bubble length were assumed to be much greater than the vessel diameter so that a cylindrical geometry was appropriate and edge effects could be ignored. The model was developed based on Fick's Law, Henry's Law and the capillary theory (see Appendix for details). The proposed model provides an analytical solution of the water ascent velocity in embolized xylem vessels, allowing the evaluation of the impact of vessel diameter and position on the ascent velocity. The model

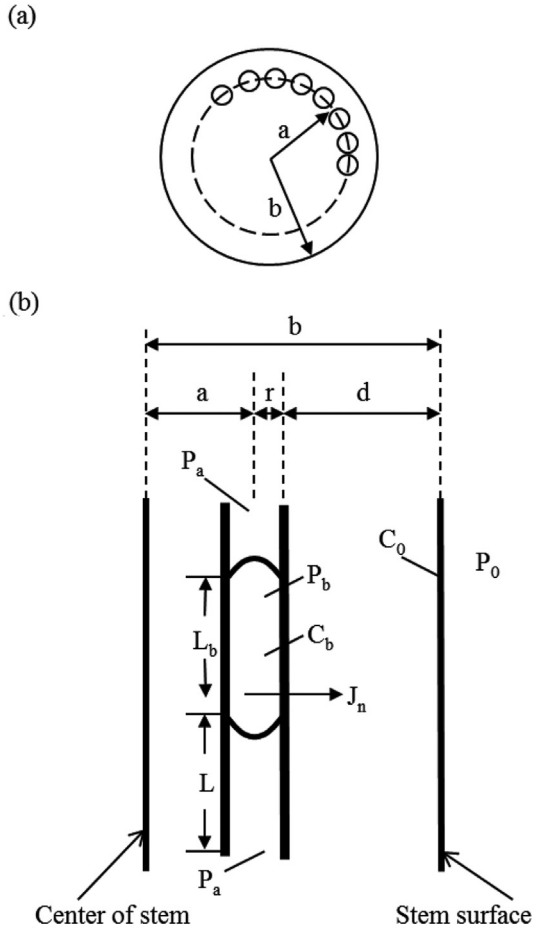

Fig. 2. Schematic of air diffusing away from a bubble inside a xylem vessel to the surface of the stem in the steady-state bubble dissolution model. (a) axial view of a stem showing the regular rings of xylem vessels (a simple geometry is assumed); (b) longitudinal view of a single embolized xylem vessel with an air bubble trapped inside (an inner vessel is illustrated here). See the appendix for more details.

is conceptually identical to that of Yang and Tyree (1992); Tyree and Yang 1992) except that the model in the Appendix was solved for meniscus velocity, which can be measured by MRI, whereas the earlier model only inferred embolism disappearance from the increase in stem-segment hydraulic conductance; hence, the previous model was solved for changes in hydraulic conductance with time (see discussion). Model calculations and experimental data for meniscus velocity are presented below.

RESULTS AND DISCUSSION

Temporal and Spatial Patterns of Water Refilling

^{1}H MRI images of the cross section of the grapevine stems water refilled at ambient xylem pressure are shown in Fig. 3; similar images were obtained for stems at 9.8 kPa. The resolution of these ^{1}H MRI images is 23 μm; at this

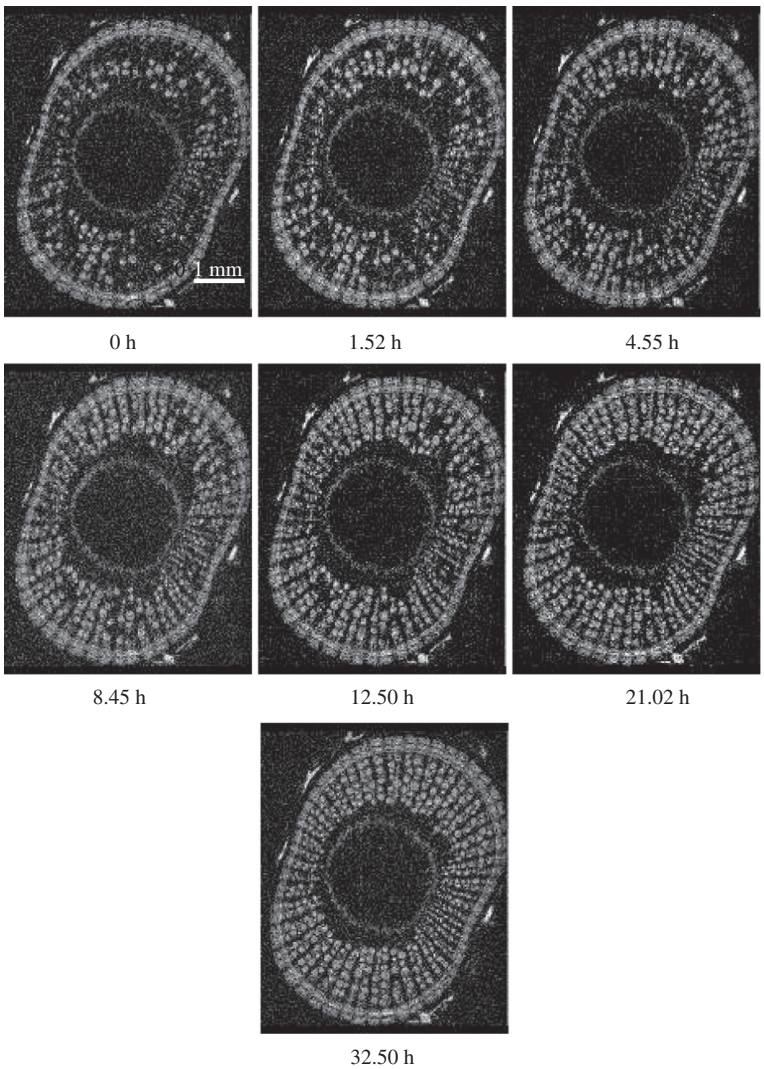

Fig. 3. ^{1}H MRI images of the cross section of a grapevine stem at different refilling times. Water refilling was performed at ambient pressure. The ^{1}H MRI images are labeled by the MRI experiment start time. For example, the first image (labeled 0 h) was acquired immediately after the water refilling experiment began.

resolution a significant portion of the xylem vessels are individually resolved. The cross-section has a rounded-rectangular shape; the tissues observable in Fig. 3 are, from outside to inside: the bark (0.2–0.3 mm thick), the wood (0.6–1.1 mm thick) and pith (2.0–2.8 mm diameter for minor and major axes, respectively). The wood contains vessels (about 1/3 of the surface) with solitary vessels surrounded by ray cells and fibers. The light areas in the image contain the highest water content and vessels appear black when air-filled. The pith appears mostly dark because the amount of water was insufficient to generate a detectable signal.

Some vessels were water filled on the first MRI scan, which is expected because flushing the stem segments with compressed air is not sufficient to push water out of ''closed'' vessels. Closed vessels connect to adjacent vessels via pit membranes and the applied gas pressure was not sufficient to push air bubbles through some pit membranes. As more vessels became water-filled, rays became visible as dark radial bands extending from the pith toward the cambium and the bark. These rays consist of living parenchyma cells. The number of water-refilled xylem vessels (white circles) could be counted at each refilling time allowing the investigation of the temporal pattern, i.e., the time course of refilling characteristic to the refilling process. A plot of the temporal pattern of the refilling process at each xylem pressure is shown in Fig. 4; as seen in this figure, the time required for complete refilling is approximately 30 h at ambient pressure and approximate 20 h at 9.8 kPa. These plots also show that more vessels are refilled at the early stage than at the late stage of the process.

The spatial pattern of the refilling process in the cross section of the stem is more easily observed by

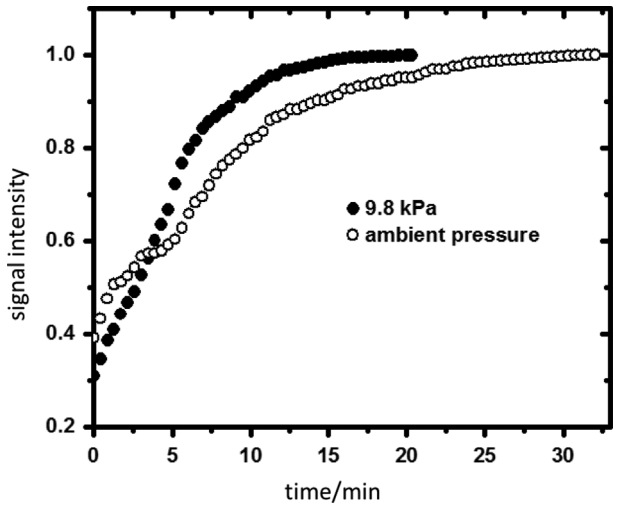

Fig. 4. Temporal information about the refilling processes at ambient pressure and at a pressure of 9.8 kPa above ambient pressure.

considering the MRI difference images, which were obtained by subtracting one MRI image from another. The MRI difference images shown in Fig. 5 correspond to the MRI images that were obtained at 9.8 kPa. Similar difference images were obtained at ambient pressure. These MRI difference images show how refilling proceeded in the cross section of the stem. Close examination of these difference images suggests that vessels close to the bark (the outer edge of the stem) tend to refill faster than do inner ones (those closer to the pith), although exceptions exist.

The innermost xylem vessels tend to be the slowest to fill (vide infra), possibly due to the formation of tyloses or gels or both (Sun et al. 2008), which both decrease the hydraulic conductivity of the vessel lumina. The model predicts that a decrease in K_h by a factor of 10^{-4} would account for the observed velocities (see Appendix). Refilling could also be by a different hydraulic path, i.e., radially from water-filled vessels to the inner-most vessels (Cirelli et al. 2008). If the radial conductivity is not sufficiently low in grape to account for the low velocity then we would postulate a large contact angle (see Eq. A12 in the Appendix) to account for the low velocity.

Since vessels of similar distance to the edge of the stem vary significantly in diameter, and since they are not in a perfectly circular ring, a clear-cut spatial pattern was not observed in the MRI experiments. Ideally, xylem vessels of identical diameter and length in a well-defined ring should be investigated to reveal whether their positions within the cross section of the stem play a significant role in refilling; such investigations could be facilitated using a theoretical model.

The earlier model of Tyree and Yang (1992; Yang and Tyree 1992), which correctly predicted the tempo of refilling in maple through its impact on hydraulic conductance, assumed that vessels refilled in an organized pattern from outermost to innermost in maple stems. However, our results suggest this assumption may be wrong since the observed refilling pattern is somewhat random; i.e., vessels deeper in the stem may be refilling simultaneously with outer vessels. Vessels that are refilling have the highest concentration of gas immediately adjacent to the bubble surface (Henry's law) and this high air concentration ought to block diffusion from vessels further inside (Fick's Law). Our results show that some air, which dissolves from inner vessels, must follow a pathway of diffusion between the outer vessels. Since maple wood vessels occupy less of the wood volume (11% of vessels by volume) than grape, the pattern of dissolution may be more scattered than grape stems.

Meniscus Ascent Velocity

An MSME MRI method as discussed in Section 2 was used to determine the water ascent velocity in each of the embolized xylem vessels. This method avoids the problem of low temporal resolution at high spatial resolution that exists in MRI velocity mapping or flow imaging experiments (Callaghan and Xia 1991; Pope and Yao 1993). As demonstrated in the previous section, the water ascent velocity varies from one xylem vessel to another. To determine the ascent velocity in individual xylem vessels, high resolution MRI experiments are required to resolve individual xylem vessels. Since the water ascent velocity in embolized xylem vessels is low, the method described below was implemented to determine its value.

As discussed above, qualitatively, the water ascent velocity can be estimated by monitoring the progress of the water meniscus within the embolized xylem vessels along the defined axial slices. For example, as shown in Fig. 6, at refilling time t_1, the meniscus in one embolized xylem vessel (highlighted by the white circle) appeared in slice 2 but was not seen in slices 3 or 4; however, by refilling time t_2 it had moved up to slice 4. Since the slice thickness and the interslice gap are known, the distance the meniscus travelled between time t_1 and t_2 is also known. If a constant water ascent velocity is assumed, its value can be calculated. To ensure a more accurate measurement of the water ascent velocity, weighting factors on the signal intensity of the ^{1}H MRI images must be considered. The ^{1}H T_1 value for water in the xylem vessels under the normal water-filled condition was 0.6–1.0 s; therefore, a TR of 3 s was used and this largely removed the T_1 weighting. T_2 was estimated to be 200 to 600 ms. To eliminate errors arising from the time required to acquire an image (i.e., the acquisition time effect), the correlation between the MRI signal intensity and the refilling time for each slice was first established; the MRI signal intensities for different slices were then compared to obtain a pair of slices that are characterized by the same MRI signal intensity at their different refilling times. For example, the signal intensities of the MRI images of slices 2 and 3 defined on a specific vessel refilled at ambient pressure for a range of refilling times were determined and are shown in Fig. 7.

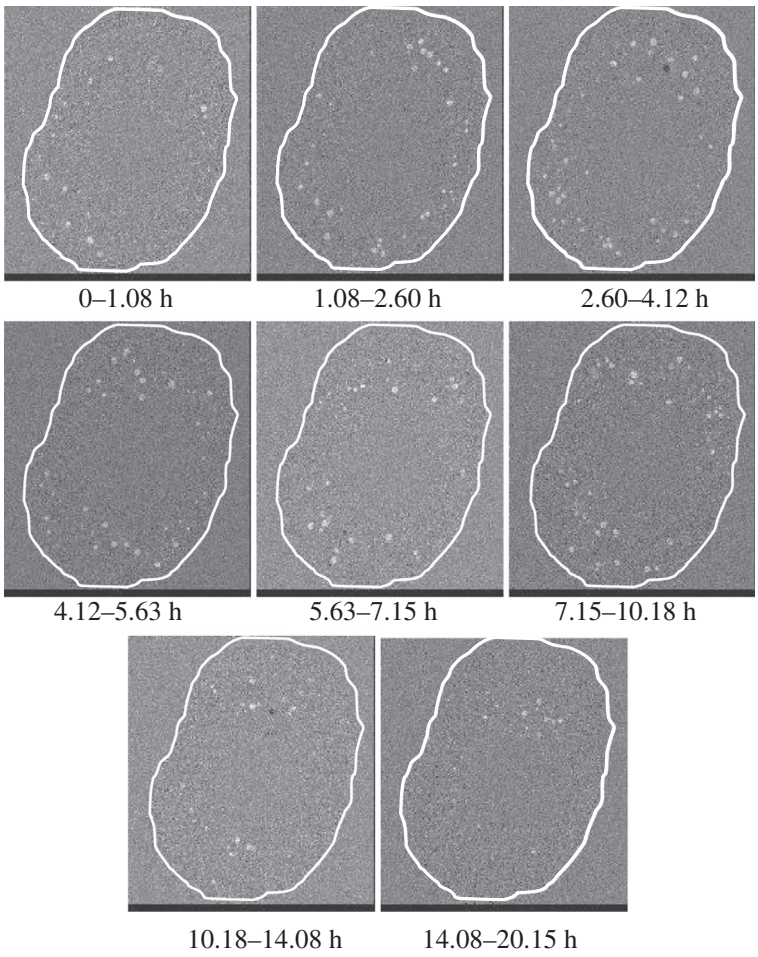

Fig. 5. Magnetic resonance imaging difference images obtained from the ^{1}H MRI images acquired with water refilling performed at 9.8 kPa above ambient pressure. The MRI difference images are labeled in such a way that, for example, the first difference image (labeled 0–1.08 h) was obtained by subtracting the ^{1}H MRI image acquired at 0 h from the one acquired at 1.08 h. For clarity, the outside edge of the stem is highlighted in white.

Signal intensities were measured based on a region of interest (ROI) defined such that it encompassed the entire lumen; the noise level was assumed to be the same for all images. If the signal intensities for two different slices of the same xylem vessel are the same, the water ascent velocity can be readily calculated without concern for the acquisition time effect since under this condition, this effect is the same for both slices and the physical displacement (i.e., slice position change) due to water ascent equals the one determined from situations where no acquisition time effect is involved. As shown in Fig. 7, the signal intensity for slice 2 at refilling time t_1 is the same as that for slice 3 at refilling time t_2. The water ascent velocity in this embolized xylem vessel is then calculated as 0.035 mm min^{-1} (0.58 μm s^{-1}) according to Eq. 1. This process can be repeated on any resolvable xylem vessel to determine the water ascent velocity within it. When analyzing the data, some high-velocity rates were encountered. For example, the water meniscus appeared in slice 1 in one experiment and then in slice 5 in another experiment 13 min later. In fact, the experimental setup used in this study will not allow the determination of an ascent velocity that is higher than 0.72 mm min^{-1}. As long as two data points could be collected for each of the two slices, the aforementioned procedure was used to determine the ascent velocity. In any case, where only one point was available for one slice or both, scaling factors, $R_i = \frac{S_i}{S_0}$, were defined where S_0 denotes the signal intensity of a slice that was fully water filled when the imaging experiment started, and $S_i = (i = 1,2)$ denotes the signal intensity of the two slices. Under these conditions, Eq. 1 becomes:

$$v = \frac{(n_2 - n_1 - 1)(l + \Delta l) + \Delta l + (1 + R_2 - R_1)l}{t_2 - t_1} \quad (2)$$

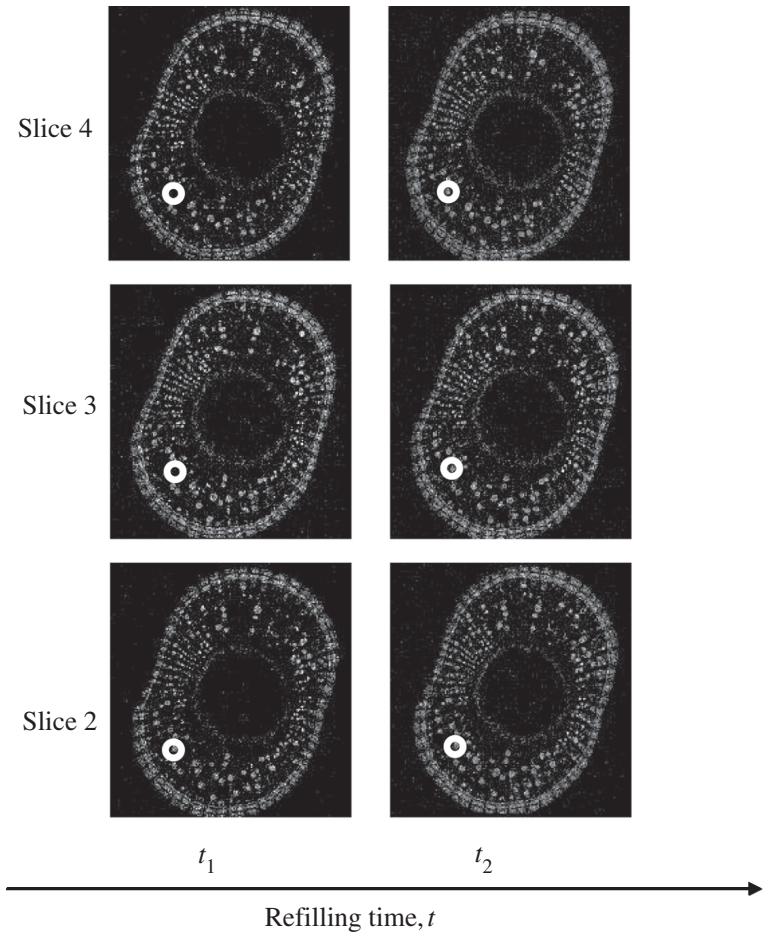

Fig. 6. Slice position and refilling time dependence of the signal intensity of the MRI images acquired in this study. The circles in the bottom left corner of each image highlight the progress of the water meniscus along the defined axial slices (see text for details).

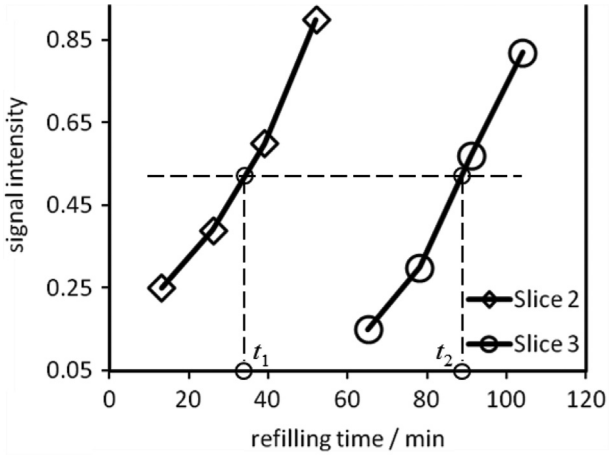

Fig. 7. Signal intensities of two slices defined on a specific xylem vessel at different refilling times. Water refilling was conducted at ambient pressure. See text for the procedure.

Velocity data for refilling at two different applied xylem pressures were determined. The ascent velocity at ambient pressure ranges from 0.0090 to 0.60 mm min^{-1} (0.15 to 10 μm s^{-1}) and that at 9.8 kPa ranges from 0.016 to 0.70 mm min^{-1} (0.27 to 12 μm s^{-1}) (Fig. 8). The broad range of velocity values is due to the inclusion of data from the innermost xylem vessels, which were slow to refill. Excluding this population of vessels, the velocity ranges from 0.020 to 0.60 mm min^{-1} (0.33 to 10 μm s^{-1}) at ambient pressure, and from 0.050 to 0.70 mm min^{-1} (0.83 to 12 μm s^{-1}) at 9.8 kPa. These values are orders of magnitude greater than those reported by Brodersen et al. (2010), who reported an estimated velocity of 6×10^{-4} μm s^{-1} and a calculated value of 0.16 μm s^{-1}. In Brodersen's study, undertaken in the summer, the refilling rate is limited by the rate at which osmotic substances can be moved from living ray cells to the droplets of water that are refilling vessels. This process may involve biochemical conversion of starch solids to sugar and transport of the sugar across cell membranes from ray cells to vessels and is

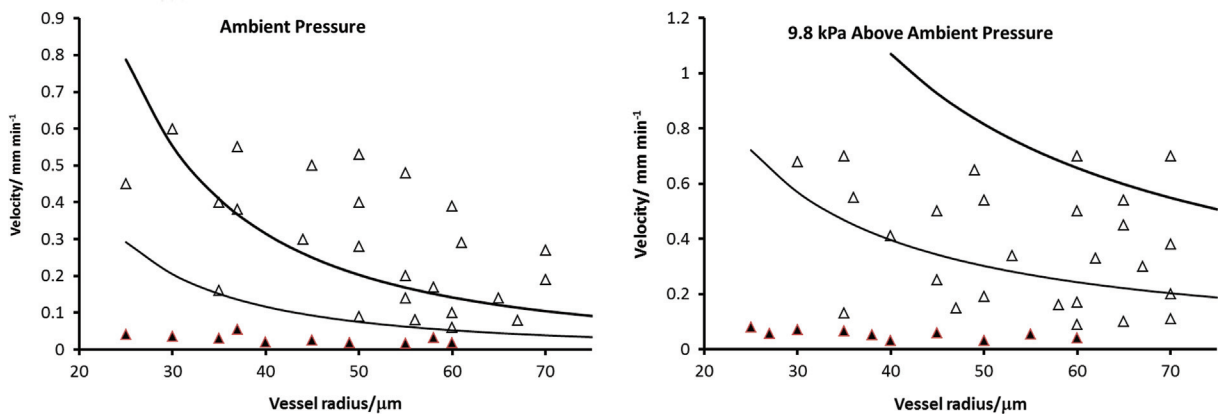

Fig. 8. Water ascent velocity as a function of vessel radius, at ambient pressure and at 9.8 kPa above ambient pressure. The uncertainty associated with the determined water ascent velocity is estimated to be 20–40%, based on the deviation in the data from a minimum of five experiments. The vessel radius was determined from the corresponding ^{1}H MRI images and the uncertainty is 10%. The open triangles represent data points from the outer vessels, while the filled triangles indicate data points from the innermost vessels. The curves are theoretical values: upper curve = velocity versus vessel radius for vessels 0.4 mm from the surface of the stem; lower curve = velocity versus vessel radius for vessels 1.4 mm from the stem surface (see appendix and Fig. 2a).

likely to be quite slow. The growth of the water volume is osmotically induced following the biochemical processes and membrane transport; hence the measured rates are quite low. In our case, stem pressurization was mechanically induced and the rate of water filling was limited by the rate of diffusion of air from the air bubbles.

Model Calculations

The steady-state bubble model has the advantage of having an analytical solution that allows the easy evaluation of the impact of vessel diameter and position on the rate of advance of the meniscus and explicitly quantifies the co-limiting influence of diffusion and hydraulic conductance on the physical processes occurring as a bubble dissolves. Results from model calculations suggest that vessel diameter and position are two important factors controlling the water ascent velocity for a given stem segment at a given refilling pressure (Fig. 8). Model calculations also indicate that the process of water refilling is limited by the diffusion process (i.e., by k_D) in which air diffuses away from inside the bubble to the edge of the stem. The proposed steady-state bubble model provides a basis for understanding the biophysical constraints of embolism repair and a benchmark for estimating the water ascent velocity in embolized xylem vessels for grapevines.

The discrepancies between the MRI-determined and the model-calculated water ascent velocities arise from at least two possible sources. One is the simple stem and xylem vessel geometry adopted in the model and the other is the uncertainty of the values for the model parameters. Most importantly, the air diffusion coefficient in woody stems and the contact angle between vessel walls and the curvature of the air-water interface are two parameters whose values have a significant influence on the predicted results.

According to theory [see the Appendix or Yang and Tyree (1992)], vessel diameter should limit the radius of curvature of the meniscus if the contact angle of the air-water interface is zero. The meniscus diameter and surface tension of the fluid determines the pressure of the bubble (Eq. A12 in the Appendix). The surface pressure of the bubble determines the concentration of the dissolved air at the bubble surface (Henry's Law) and surface concentration determines the rate of diffusion away from the surface and hence the velocity of the meniscus (Fick's Law).

A possible explanation for the poor correlation between meniscus velocities and diameter is that the MRI images might give incorrect diameter data. To investigate, the radius of all vessels >25 μm in similar grape stems were measured using a light microscope; a mean and standard deviation of 51 ± 38 ($N = 386$) was found, which compared well with the values in Fig. 8 (49 ± 13, $N = 35$) (Dr. Jing Cai, personal communication).

The time for bubble dissolution increases with increasing vessel diameter. The high variability shown in Fig. 8 suggests that other parameters must also influence the refilling process significantly and these effects may cancel out the vessel size effect on water refilling. For instance, if an air bubble trapped inside a xylem vessel disappears through dissolution into water and subsequently diffuses away from within the vessel to the outside of the stem, then the vessel position within the cross section of the stem is expected to influence the ascent velocity because this position determines the length of the diffusion pathway from the center of the vessel to the surface of the stem. To evaluate the effect of vessel size on the ascent velocity, a regular vessel arrangement within the cross section of the stem is necessary. Once again,

because ideal uniform vessels do not exist, one is limited to theoretical modeling.

Model Versus Reality

The advantage of the model developed in the Appendix is that it predicts how fast bubbles entrapped in vessels will collapse assuming only passive physical processes are occurring (i.e., experimental artifacts do not affect the calculations). The speed of bubble collapse is measured by the velocity of the air/water interface. The derivation allows for two types of limitation of bubble collapse, i.e., diffusion-limitation (Fick's law) and mass-flow limitation (Hagen–Poiseuille law), which is of negligible impact and will be ignored for the remainder of this discussion.

The diffusion rate is controlled by both the driving force and the rate constant imposed by Fick's law of diffusion (Callaghan 2011). The driving force is determined by the difference between the bubble pressure and the atmospheric air pressure (P_b - P_o) and the rate constant is given by k_D (see Eq. A2). This equation includes the coefficient of diffusion (D) of "air" in the mix of the water/cell wall and some terms for the diffusion path length and geometry. The exact D is an unknown quantity in the context of wood, which consists of water-filled vessel-lumina, cell walls and a mix of living cells along the pathway of diffusion. The theoretical values of v are within a factor of 2 or 3 of the observed values. The velocities of the innermost vessels (solid triangles in Fig. 8) are slower than expected from the model (for reasons stated above). In contrast the outermost large vessels refill faster than predicted by theory (open triangles Fig. 8). Since the temperature of the gradient coils was maintained at 20°C, the varying refilling time is thought to be a property of the stems and not an experimental artifact arising from temperature gradients. The model assumes that vessels are in uniform concentric rings (five in the grape stems used in this experiment, see Fig. 3) and that all vessels are the same radius within a ring for any one solution (see the curves in Fig. 8). If all vessels were of the same radius in all five rings then the outer rings would have the highest v and its value would decrease gradually to the lowest values in the inner ring. Indeed, the inner ring has the lowest experimental values of v but there is little correlation with the outer four rings (Fig. 8). The ring-location of a vessel determines the value of k_D but the radius of the vessel within a ring determines P_b (bubble pressure) and hence the driving force. Also note that the vessel r value is variable in any given ring hence the bubble pressure of a small vessel radius will exceed the bubble pressure of a large vessel radius. Thus, small vessels might collapse very quickly because of the possible rapid diffusion of air between a small vessel and an adjacent large vessel within the same ring or in an adjacent ring. This process might account for the scattered values of v in Fig. 8 and indicates that the model needs to be improved to include the spatial effects. However, this vessel-size affect does not explain the high-velocity values of the large vessels in the upper right corner of Fig. 8, because if air moved quickly from small vessels to large vessels the v of the small vessels would increase at the expense of a decrease in v of large vessels. The current model is one-dimensional, radial, and assumes cylindrical geometry and a near steady state, whereas a better model would be a two-dimensional finite element model assuming a non-steady state. However, it is unclear if a more complex model would allow one to determine if the measured values of v exceed what would be expected for a purely physical process involving Henry's law, Fick's law, surface tension and the Hagen–Poiseuille law. Fortunately there is a more powerful test that might address this question.

That test involves measuring how v increases in response to a known change in P_b (Fig. 8). At ambient pressure (upper plot) the bubble pressure is $P_b \approx (2\tau\cos(\phi))/r$, but at 9.8 kPa above ambient pressure, $P_b \approx P_a + (2\tau\cos(\phi))/r$ (lower plot). Surface tension determines the value of $(2\tau\cos(\phi))/r$, which is uncertain because the contact angle ϕ is unknown, but it is likely to be the same at both pressures. Also k_D is the same in both cases, hence the ratio of velocities, v_{ratio}, should be given by:

$$v_{ratio} = \frac{P_a + 2\tau\cos(\phi)/r}{2\tau\cos(\phi)/r} = \frac{P_a}{2\tau\cos(\phi)/r} + 1 \geq \frac{P_a}{2\tau/r} + 1 \quad (3)$$

because $(\cos(\phi) \leq 1)$.

Mean values of $2\tau/r$ were calculated for the inner ring of vessels and for all vessels. At ambient pressure, the mean value of $2\tau/r$ is 3.58 kPa for the inner ring of vessels and 3.18 kPa for all rings, but for 9.8 kPa above ambient pressure, $P_a = 9.8$ kPa so the minimum ratio of pressures is 3.73 for the inner ring and 4.1 for all the vessels. However, the mean ratio of velocities is 1.86 for the inner ring of vessels and 1.36 for all the vessels. Hence the applied pressure enhances the refilling process less than expected from theory. This may mean that the rate of refilling of the stem is more than might be expected from purely physical processes when there is no external applied pressure. The nature of the additional processes must await elucidation by future studies, but the findings on excised stem segments are consistent with previous studies on intact grape vines.

CONCLUSIONS

High-resolution ^{1}H MRI experiments were conducted to investigate the temporal and spatial patterns of water refilling of embolized xylem vessels in grapevine stems. Magnetic resonance imaging difference images indicate that vessel position within the cross section of the stem may influence the refilling process within the xylem although a clear correlation was not observed due to the fact that vessels are of varying sizes and are not regularly arranged in the stems. An MRI method for determining the water ascent velocity in individual embolized xylem

vessels was developed and used to obtain water ascent velocity data at two different applied xylem pressures. A steady-state bubble model was developed to calculate the water ascent velocity in embolized xylem vessels and calculations based on this model show that vessel diameter and position have significant influences on the water ascent velocity. Our results tentatively point toward a process that speeds up the rate of bubble collapse even in excised stem segments of grape plants, but the mechanism behind this speed up is not clearly understood. The experimentally obtained water ascent velocity data, together with the proposed steady-state bubble model, provide important information about water refilling and are likely to lead to an improved understanding of embolism repair. As well, we have provided an example demonstrating how NMR imaging at sub-millimeter resolution allows scientists to investigate water density and dynamics in plants. We hope this work will encourage these scientists to consider MRI as a useful imaging tool for studying these and other phenomena in plants.

ACKNOWLEDGMENTS

The authors thank Dr. Guy Bernard and other members of the solid-state NMR group at the University of Alberta for helpful discussions and comments. MW thanks the University of Alberta for funding. REW is a Canada Research Chair in Physical Chemistry and would like to thank the Natural Sciences and Engineering Research Council, NSERC, of Canada for financial support. This research was made possible by research grants from an NSERC Discovery Grant held by MTT who also wishes to thank the United States Forest Service for salary support while working at the University of Alberta. We also thank Dr. Uwe Hacke for bringing about our collaboration and for consultation and encouragement during all phases of research and writing. Finally, we acknowledge the efforts of three anonymous reviewers whose comments helped improve this manuscript.

Araujo, C. D., MacKay, A. L., Whittall, K. P. and Hailey, J. R. T. 1993. A diffusion model for spin-spin relaxation of compartmentalized water in wood. J. Magn. Reson. B **101**: 248–261.

Arbabi, A. and Mastikhin, I. V. 2012. Magnetic susceptibility based magnetic resonance estimation of micro-bubble size for the vertically upward bubbly flow. J. Magn. Reson. **225**: 36–45.

Beyea, S. D., Balcom, B. J., Mastikhin, I. V., Bremner, T. W., Armstrong, R. L. and Grattan-Bellew, P. E. 2000. Imaging of heterogeneous materials with a turbo spin echo single-point imaging technique. J. Magn. Reson. **144**: 255–265.

Blümich, B. 2000. NMR imaging of materials. Oxford University Press, New York, NY.

Borghetti, M., Edwards, W. R. N., Grace, J., Jarvis, P. G. and Raschi, A. 1991. The refilling of embolized xylem in *Pinus sylvestris* L. Plant Cell Environ. **14**: 357–369.

Borisjuk, L., Rolletschek, H. and Neuberger, T. 2012. Surveying the plant's world by magnetic resonance imaging. Plant J. **70**: 129–146.

Brodersen, C. R., McElrone, A. J., Choat, B., Matthews, M. A. and Shackel, A. 2010. The dynamics of embolism repair in Xylem: *in vivo* visualizations using high-resolution computed tomography. Plant Physiol. **154**: 1088–1095.

Brodribb, T. J. 2009. Xylem hydraulic physiology: the functional backbone of terrestrial plant productivity. Plant Sci. **177**: 245–251.

Callaghan, P. T. 1990. Susceptibility-limited resolution in nuclear magnetic resonance microscopy. J. Magn. Reson. **87**: 304–318.

Callaghan, P. T. 1991. Principles of nuclear magnetic resonance microscopy. Oxford University Press, New York, NY.

Callaghan, P. T. 2011. Translational dynamics & magnetic resonance. Principles of pulsed gradient spin echo NMR. Oxford University Press, Oxford, UK.

Callaghan, P. T. and Xia, Y. 1991. Velocity and diffusion imaging in dynamic NMR microscopy. J. Magn. Reson. **91**: 326–352.

Canny, M. J. 1998. Applications of the compensating pressure theory of water transport. Am. J. Bot. **85**: 897–909.

Choat, B., Drayton, W. M., Brodersen, C., Matthews, M. A., Shackel, K. A., Wada, H. and McElrone, A. J. 2010. Measurement of vulnerability to water stress-induced cavitation in grapevine: a comparison of four techniques applied to a long-vesseled species. Plant Cell Environ. **33**: 1502–1512.

Cirelli, D., Jagels, R. and Tyree, M. T. 2008. Toward an improved model of maple sap exudation: the location and role of osmotic barriers in sugar maple, butternut and white birch. Tree Physiol. **28**: 1145–1155.

Clearwater, M. J. and Clark, C. J. 2003. In vivo magnetic resonance imaging of xylem vessel contents in woody lianas. Plant Cell Environ. **26**: 1205–1214.

Clearwater, M. J. and Goldstein, G. 2005. Embolism repair and long distance water transport. Pages 375-399 *in* N. M. Holbrook and M. A. Zwieniecki, eds. Vascular transport in plants. Elsevier Academic Press, London, UK.

De Deene, Y. and Baldock, C. 2002. Optimization of multiple spin–echo sequences for 3D polymer gel dosimetry. Phys. Med. Biol. **47**: 3117–3141.

Facette, M. R., McCully, M. E., Shane, M. W. and Canny M. J. 2001. Measurements of the time to refill embolized vessels. Plant Physiol. Biochem. **39**: 59–66.

Graumann, R., Oppelt, A. and Stetter, E. 1986. Multiple-spin-echo imaging with a 2D Fourier method. Magn. Reson. Med. **3**: 707–721.

Gruwel, M. L. H., Latta, P., Sboto-Frankenstein, U. and Gervai, P. 2013. Visualization of water transport pathways in plants using diffusion tensor imaging. Prog. Electromagn. Res. C **35**: 73–82.

Hacke, U. G. and Sperry, J. S. 2003. Limits to xylem refilling under negative pressure in *Laurus nobilis* and *Acer negundo*. Plant Cell Environ. **26**: 303–311.

Holbrook, N. M. and Zwieniecki, M. A. 1999. Embolism repair and xylem tension: do we need a miracle? Plant Physiol. **120**: 7–10.

Holbrook, N. M., Ahrens, E. T., Burns, M. J. and Zwieniecki, M. A. 2001. In vivo observation of cavitation and embolism repair using magnetic resonance imaging. Plant Physiol. **126**: 27–31.

Homan, N. M., Windt, C. W., Vergeldt, F. J., Gerkema, E. and Van As, H. 2007. 0.7 and 3 T MRI and sap flow in intact trees: xylem and phloem in action. Appl. Magn. Reson. **32**: 157–170.
Kimmich, R. 1997. NMR: Tomography, diffusometry, relaxometry. Springer-Verlag, Berlin, Germany.
Köckenberger, W., Pope, J. M., Xia, Y., Jeffrey, K. R., Komor, E. and Callaghan, P. T. 1997. A non-invasive measurement of phloem and xylem water flow in castor bean seedlings by nuclear magnetic resonance microimaging. Planta **201**: 53–63.
Laschimke, R., Burger, M. and Vallen, H. 2006. Acoustic emission analysis and experiments with physical model systems reveal a peculiar nature of the xylem tension. J. Plant Physiol. **163**: 996–1007.
Lee, S.-J. and Kim, Y. 2008. In vivo visualization of the water-refilling process in xylem vessels using X-ray micro-imaging. Ann. Bot. **101**: 595–602.
MacFall, J. S. and Johnson, G. A. 2012. Plants, seeds, roots, and soils as applications of magnetic resonance microscopy. Vol. 6, pages 3403–3409 *in* R. K. Harris and R. E. Wasylishen, eds. Encyclopedia of NMR. John Wiley & Sons, Chichester, UK.
Markley, J. L., Horsley, W. J. and Klein, M. P. 1971. Spin-lattice relaxation measurements in slowly relaxing complex spectra. J. Chem. Phys. **55**: 3604–3605.
McCully, M. E., Huang, C. X. and Ling, L. E. C. 1998. Daily embolism and refilling of xylem vessels in the roots of field-grown maize. New Phytol. **138**: 327–342.
McElrone, A. J., Brodersen, C. R., Alsina, M. M., Drayton, W. M., Matthews, M. A., Shackel, K. A., Wada, H., Zufferey, V. and Choat, B. 2012. Centrifuge technique consistently overestimates vulnerability to water stress-induced cavitation in grapevines as confirmed with high-resolution computed tomography. New Phytol. **196**: 661–665.
Meiboom, S. and Gill, D. 1958. Modified spin-echo method for measuring nuclear relaxation times. Rev. Sci. Instrum. **29**: 688–691.
Melcher, P. J., Goldstein, G., Meinzer, F. C., Yount, D. E., Jones, T. J., Holbrook, N. M. and Huang, C. X. 2001. Water relations of coastal and estuarine *Rhizophora mangle*: xylem pressure potential and dynamics of embolism formation and repair. Oecologia **126**: 182–192.
Narasimhan, P. T. and Jacobs, R. E. 2005. Microscopy in magnetic resonance imaging. Annu. Rep. NMR Spectrosc. **55**: 259–297.
Pate, J. S. and Canny, M. J. 1999. Quantification of vessel embolisms by direct observation: a comparison of two methods. New Phytol. **141**: 33–44.
Pérez-Donoso, A. G., Greve, L. C., Walton, J. H., Shackel, K. A. and Labavitch, J. M. 2007. *Xylella fastidiosa* infection and ethylene exposure result in xylem and water movement disruption in grapevine shoots. Plant Physiol. **143**: 1024–1036.
Pope, J. M. and Yao, S. 1993. Quantitative NMR imaging of flow. Conc. Magn. Reson. **5**: 281–302.
Raven, J. A. 1977. The evolution of vascular land plants in relation to supracellular transport processes. Adv. Bot. Res. **5**: 153–219.
Rokitta, M., Zimmermann, U. and Haase, A. 1999. Fast NMR flow measurements in plants using FLASH Imaging. J. Magn. Reson. **137**: 29–32.
Roscher, A., Emsley, L. and Roby, C. 1996. The effect of imperfect saturation in saturation-recovery T_1 measurements. J. Magn. Reson. A **118**: 108–112.
Salleo, S., Lo Gullo, M. A., de Paoli, D. and Zippo, M. 1996. Xylem recovery from cavitation-induced embolism in young plants of *Laurus nobilis*: a possible mechanism. New Phytol. **132**: 47–56.
Salleo, S., Trifilò, P., Esposito, S., Nardini, A. and Lo Gullo, M. A. 2009. Starch-to-sugar conversion in wood parenchyma of field-growing *Laurus nobilis* plants: a component of the signal pathway for embolism repair? Funct. Plant Biol. **36**: 815–825.
Scheenen, T. W. J., Vergeldt, F. J., Heemskerk, A. M. and Van As, H. 2007. Intact plant magnetic resonance imaging to study dynamics in long-distance sap flow and flow-conducting surface area. Plant Physiol. **144**: 1157–1165.
Sun, Q., Rost, T. L. and Matthews, M. A. 2008. Wound-induced vascular occlusions in *Vitis vinifera* (Vitaceae): tyloses in summer and gels in winter. Am. J. Bot. **95**: 1498–1505.
Telkki, V.-V. 2012. Wood characterization by NMR and MRI of fluids. Vol 9, pages 5413–5420 *in* R. K. Harris and R. E. Wasylishen, eds. Encyclopedia of NMR. John Wiley & Sons, Chichester, UK.
Tyree, M. T. and Sperry, J. S. 1989. Vulnerability of xylem to cavitation and embolism. Annu. Rev. Plant Physiol. Mol. Biol. **40**: 19–38.
Tyree, M. T. and Yang, S. 1992. Hydraulic conductivity recovery versus water pressure in xylem of *Acer saccharum*. Plant Physiol. **100**: 669–676.
Tyree, M. T. and Zimmermann, M. H. 2002. Xylem structure and the ascent of sap. 2nd ed. Springer, Heidelberg, Germany.
Tyree, M. T., Salleo, S., Nardini, A., Lo Gullo, M. A. and Mosca, R. 1999. Refilling of embolized vessels in young stems of laurel. Do we need a new paradigm? Plant Physiol. **120**: 11–21.
Van As, H., Scheenen, T. and Vergeldt, F. J. 2009. MRI of intact plants. Photosynth. Res. **102**: 213–222.
Windt, C. W., Vergeldt, F. J., Adrie de Jager, P. and Van As, H. 2006. MRI of long-distance water transport: a comparison of the phloem and xylem flow characteristics and dynamics in poplar, castor bean, tomato and tobacco. Plant Cell Environ. **29**: 1715–1729.
Yang, L.-J., Yao, T.-J. and Tai, Y.-C. 2004. The marching velocity of the capillary meniscus in a microchannel. J. Micromech. Microeng. **14**: 220–225.
Yang, S. and Tyree, M. T. 1992. A theoretical model of hydraulic conductivity recovery from embolism with comparison to experimental data on *Acer saccharum*. Plant Cell Environ. **15**: 633–643.
Zwieniecki, M. A. and Holbrook, N. M. 1998. Diurnal variation in xylem hydraulic conductivity in white ash (*Fraxinus americana* L.), red maple (*Acer rubrum* L.) and red spruce (*Picea rubens* Sarg.). Plant Cell Environ. **21**: 1173–1180.
Zwieniecki, M. A. and Holbrook, N. M. 2000. Bordered pit structure and vessel wall surface properties. Implications for embolism repair. Plant Physiol. **123**: 1015–1020.

Appendix

Start from the steady-state Fick's Law:

$$J_n = k_D(C_b - C_0) \tag{A1}$$

where J_n is the steady-state flux in mol s^{-1} per vessel, C_b is the concentration of air dissolved in the water at the bubble surface (mol m^{-3}), and C_0 is the concentration of air dissolved in water at the stem surface. k_D is a diffusion constant that can be defined (Eq. A2) in terms of steady-state diffusion from a cylindrical surface with a single vessel in the center:

$$k_D = \frac{2\pi DL_b}{\ln(b/a)} \tag{A2}$$

where L_b is the length of the bubble in the vessel, a is the radial distance from the center of the stem to the ring of vessels, b is the radial distance from the center of the stem to the stem surface, and D is the diffusion coefficient for air in the stem. For diffusion from a ring of vessels, k_D can be defined as:

$$k_D = \frac{2\pi DL_b}{\ln(b/a)N} \tag{A3}$$

where N is the number of vessels in the ring that can be calculated from:

$$N = f\frac{\pi a}{r} \tag{A4}$$

where r is the vessel radius and f is the fraction of the ring circumferance ($2\pi a$) that is occupied by the sum of vessels diameters ($f = 0.5$) in this paper. By introducing Henry's Law of gas solubility, Eq. A1 can be expressed in terms of bubble pressure:

$$J_n = \frac{k_D}{H}(P_b - P_o) \tag{A5}$$

where H is the gas solubility coefficient, P_b is the absolute pressure of the air in the bubble, and P_o is the barometric pressure.

The ideal gas law states:

$$P_b V_b = nRT \tag{A6}$$

Hence

$$\frac{dV_b}{dt} = \frac{dn}{dt}\frac{RT}{P_b} = -J_n\frac{RT}{P_b} \tag{A7}$$

The minus sign results from the fact that $dn/dt < 0$ and $J_n > 0$. If we define $J_v = -dV_b/dt$, we have:

$$J_v = J_n\frac{RT}{P_b} \tag{A8}$$

Combining Eqs. A5 and A8:

$$J_v = \frac{RT}{P_b}\frac{k_D}{H}(P_b - P_o) \tag{A9}$$

We assume water flows only from the water bottle to the lower end of the stem segment because the upper end is plugged (Fig. 1a). As the volume of the bubble contracts an equal volume of water must flow through the vessel to the bubble surface hence we can express J_v also in terms of the Hagen-Poiseuille Law:

$$J_v = \frac{k_h}{L}(P_a - P^*) \tag{A10}$$

where k_h is the hydraulic conductivity of the vessel, P^* is the absolute pressure of the fluid at the air/water interface of the bubble, P_a is the pressure of the fluid at the base of the stem and L is the path length from the base of the stem to the lower bubble surface.

$$k_h = \frac{\pi r^4}{8\eta} \tag{A11}$$

where η is the viscosity of water. The bubble pressure (P_b) is more than the adjacent fluid pressure because of the action of the surface tension of water (τ) confined to a vessel of radius $= r$ with a contact angle between the liquid and the vessel wall of ϕ degrees; hence

$$P^* = P_b - \frac{2\tau\cos(\phi)}{r} \tag{A12}$$

Thus, from Eqs. A10 and A12:

$$J_v = \frac{k_h}{L}\left(P_a - P_b + \frac{2\tau\cos(\phi)}{r}\right) \tag{A13}$$

Solving for P_b:

$$P_b = P_a + \frac{2\tau\cos(\phi)}{r} - J_v\frac{L}{k_h} \tag{A14}$$

Inserting Eq. A14 into Eq. A9 and rearranging, we obtain a quadratic equation for J_v that expresses how J_v is limited by both k_D and k_h.

$$\frac{L}{k_h}J_v^2 - \left[\frac{RTk_D}{H}\frac{L}{k_h} + P_a + \frac{2\tau\cos(\phi)}{r}\right]J_v + \frac{RTk_D}{H}\left(P_a - P_o + \frac{2\tau\cos(\phi)}{r}\right) = 0 \tag{A15}$$

The quadratic Eq. A15 can be solved analytically to obtain J_v, which is directly correlated to the water ascent velocity by:

$$J_v = \pi r^2 v \tag{A16}$$

where v denotes the water ascent velocity in embolized xylem vessels.

$$v = \frac{J_v}{\pi r^2} \tag{A17}$$

The quadratic solution may be approximated by Eq. A18 because the third term in Eq. A14 is much smaller than the first two; $J_vL/K_h =$ the pressure drop induced by laminar flow of fluid from the base of the stem segment to the lower bubble surface from Eq. A10. The maximum flow velocity observed in our study is 0.7 mm $min^{-1} = 1.2 \times 10^{-5}$ m s^{-1}. The largest pressure drop would occur in the smallest vessels (25 μm) so $J_v = 2.29 \times 10^{-14}$ m^3 s^{-1} (Eq. A16) and the computed pressure drop is 3 Pa (Eq. A10). This is 3 orders of magnitude less than the rise in pressure from surface tension (5760 Pa $= 2\tau/r$) with $\cos(\phi) = 1$ in Eq. (A10). For vessels with $r = 50$ μm, the pressure drop is almost 4 orders of magnitude. Hence a very close approximation of the solution results by substituting $P_b \cong P_a + \frac{2\tau\cos(\phi)}{r}$ into Eq. A9 to yield

$$J_v \cong \frac{RT}{P_a - \frac{2\tau\cos(\phi)}{r}}\frac{k_D}{H}\left(P_a + \frac{2\tau\cos(\phi)}{r} - P_o\right) \tag{A18}$$

The water ascent velocity in the embolized xylem vessels of grapevine stems refilled at 9.8 kPa and ambient pressure was calculated from Eq. A17, as shown in Fig. 8. Values for J_v from Eq. A18 and hence of v from Eq. A17 can only be calculated for specific values of the contact angle ϕ, which are not know experimentally. Plots shown in Fig. 8 are those obtained for $\phi = 0$. Values of the constants and parameters are shown in Table A1.

Table A1. Definition and values of constants used for the calculation of water ascent velocity[z]

Constant definition			Parameter
D_a	Air diffusivity in water	(25°C)	9.42×10^{-10} m^2 s^{-1}
R	Gas constant		8.314 m^3 Pa mol^{-1} K^{-1}
τ	Surface tension of water	(25°C)	7.2×10^{-2} N m^{-1}
H	air solubility in water	(25°C)	1.31×10^5 m^3 Pa mol^{-1}
η	Viscosity of water		1.002×10^{-3} Pa s

[z]For model calculations the number of vessels in a ring (Eq. 4) was calculated using a value of $f = 0.5$ because vessels occupy about 1/2 of the circumference $2\pi a$ in Fig. 2a.